Planck 's Dusty GEMS: VII. Atomic carbon and molecular gas in dusty starburst galaxies at z = 2 to 4

(article starts on next page)

Astronomy
&
Astrophysics

Planck's Dusty GEMS

VII. Atomic carbon and molecular gas in dusty starburst galaxies at *z* = 2 to 4[⋆]

N. P. H. Nesvadba[1], R. Cañameras[2], R. Kneissl[3,4], S. Koenig[5], C. Yang[3], E. Le Floc'h[6], A. Omont[7], and D. Scott[8]

(Affiliations can be found after the references)

ABSTRACT

The bright $^3P_1$–$^3P_0$ ([CI] 1–0) and $^3P_2$–$^3P_1$ ([CI] 2–1) lines of atomic carbon are becoming more and more widely employed as tracers of the cold neutral gas in high-redshift galaxies. Here we present observations of these lines in the 11 galaxies of the set of *Planck*'s Dusty GEMS, the brightest gravitationally lensed galaxies on the extragalactic submillimeter sky probed by the *Planck* satellite. We have [CI] 1–0 and [CI] 2–1 measurements for seven and eight of these galaxies, respectively, including four galaxies where both lines have been measured. We use our observations to constrain the gas excitation mechanism, excitation temperatures, optical depths, atomic carbon and molecular gas masses, and carbon abundances. Ratios of L_{CI}/L_{FIR} are similar to those found in the local universe, and suggest that the total cooling budget through atomic carbon has not significantly changed in the last 12 Gyr. Both lines are optically thin and trace 1–$6 \times 10^7 \, M_\odot$ of atomic carbon. Carbon abundances, X_{CI}, are between 2.5 and 4×10^{-5}, for an ultra-luminous infrared galaxy (ULIRG) CO-to-H_2 conversion factor of $\alpha_{CO} = 0.8 \, M_\odot / [\text{K km s}^{-1} \text{ pc}^2]$. Ratios of molecular gas masses derived from [CI] 1–0 and CO agree within the measurement uncertainties for five galaxies, and agree to better than a factor of two for another two with [CI] 1–0 measurements, after carefully taking CO excitation into account. This does not support the idea that intense, high-redshift starburst galaxies host large quantities of "CO-dark" gas. These results support the common assumptions underlying most molecular gas mass estimates made for massive, dusty, high-redshift starburst galaxies, although the good agreement between the masses obtained with both tracers cannot be taken as independent confirmation of either α_{CO} or X_{CI}.

Key words. galaxies: high-redshift – galaxies: formation – galaxies: starburst – galaxies: abundances

1. Introduction

Numerous observations in recent years have firmly established that the vigorous star-formation episodes in massive, dusty starburst galaxies at redshifts $z \geq 2$, which form most of the stellar populations in these galaxies within a few hundred million years, are fueled by massive reservoirs of dense molecular gas (e.g., Tacconi et al. 2008; Ivison et al. 2011; Riechers et al. 2013, see Solomon & Vanden Bout 2005 and Carilli & Walter 2013 for reviews). The physical and kinematic properties of this gas, such as densities and mass surface densities, temperatures, and bulk and turbulent motion, are critical for understanding the regulation of and upper limits imposed on the vigorous star formation up to the highest star-formation rates found in the universe.

Thanks to the new generation of wide-band millimeter and sub-millimeter receivers, and sensitive interferometers like ALMA and IRAM's NOEMA, we are now able to study these gaseous reservoirs in galaxies in the early universe at an interesting level of detail, extending and complementing the classical CO emission-line studies through observations of additional tracers. This includes the fine-structure lines of atomic or singly ionized carbon, [CI] and [CII], which are excellent tracers of the cold neutral gas in galaxies, and various other tracers of denser gas. Beuther et al. (2016) argue that [CI] is the best tracer of the cold neutral medium because [CII] can also be associated with ionized gas whereas CO emission only probes fairly dense molecular gas, and misses more diffuse gas that is however seen in [CI]. Goldsmith et al. (2012) even argue that [CI] emission

can be associated with low-excitation gas seen in [CII] absorption, as also found observationally in the Milky Way (Gerin et al. 2015) and at high redshift in the Garnet (PLCK_G045.1+61.1, Nesvadba et al. 2016), a source whose [CI] properties we also discuss here. Lines of [CI], [CII], and CO are therefore complementary probes of the gas in high-redshift galaxies.

Atomic carbon, specifically, is probed through two bright transitions, $^3P_1$–$^3P_0$, ([CI] 1–0), and $^3P_2$–$^3P_1$ ([CI] 2–1) at rest-frame frequencies of 492.1607 GHz and 809.3435 GHz, respectively, which are conveniently redshifted into the millimeter and lower sub-millimeter regime for redshifts $z \sim 2$–4. With upper level energies of $E_{up,10} = 24.2$ K and $E_{up,21} = 62.5$ K, and critical densities of about 10^3 cm^{-3}, they are easily excited over large ranges in gas density and temperature, from fairly diffuse gas (Phillips & Huggins 1981; Gerin & Phillips 2000; Goldsmith et al. 2012) to gas within dense molecular clouds (Papadopoulos et al. 2004). This makes them useful global probes of the cold neutral medium in very high-redshift galaxies. Perhaps most importantly, both [CI] lines remain optically thin even in very dusty, vigorous starburst galaxies, which is a clear advantage for mass estimates ensuring that mass scales linearly with line luminosity. However, other systematic uncertainties remain, such as those related to the carbon abundance, with uncertainties of factors of a few (e.g., Alaghband-Zadeh et al. 2013). Observations of CO, in contrast, are notoriously plagued by uncertainties related to most of the gas being hidden within optically thick clouds. This adds considerable uncertainty when generalizing the results of these observations to the overall molecular gas component in galaxies, without falling back on empirical relationships whose use cannot always be justified easily for each individual galaxy and analysis.

The [CI] fine structure lines also arise from physically relatively simple systems, meaning that many of their physical characteristics can be calculated directly from their observed properties and measured brightness temperatures or line fluxes; for example, masses and abundances, or their contribution to the cooling budget. Several studies also suggest that they are less sensitive than CO to variations in metallicity (which can lead to significant reservoirs of so-called "CO-dark" gas, e.g., Wolfire et al. 2010; Bolatto et al. 2013; Rémy-Ruyer et al. 2015; Balashev et al. 2017), abundance ratios, for example due to enhanced cosmic ray fluxes (Roueff & Flower 1992; Papadopoulos et al. 2004; Bisbas et al. 2015, 2017), X-ray heating from AGN (Meijerink et al. 2007), or molecule destruction in shocks (e.g., Krips et al. 2016). Furthermore, Papadopoulos et al. (2004) and Papadopoulos & Greve (2004) established the [CI] 1–0 line as a tracer of gas in high-redshift galaxies that seems to be well mixed with the molecular gas.

A number of studies have therefore targeted atomic carbon in high-redshift galaxies, ranging from the ground-work laid by Brown & Vanden Bout (1992), Barvainis et al. (1997), and Weiß et al. (2005a), for example, to more recent studies, in particular of strongly gravitationally lensed starburst galaxies selected in the infrared (Walter et al. 2011; Alaghband-Zadeh et al. 2013; Bothwell et al. 2017; Yang et al. 2017; Andreani et al. 2018). Such studies found luminous line emission in either one or both lines. They also showed that atomic carbon can remain optically thin out to the highest gas-mass surface densities and star-formation rates, and is consistent with high carbon abundances of a few times 10^{-5}, similar to those found in low-redshift galaxies (Gerin & Phillips 2000; Weiß et al. 2001; Israel & Baas 2002, 2003). This suggests that they have high metallicities akin to the solar value, with little difference between starburst galaxies and quasars (Alaghband-Zadeh et al. 2013). The [CI] lines, combined with other far-infrared (FIR) and millimeter emission lines, also provide interesting constraints on the gas density and strength of UV radiation fields within star-forming regions (e.g., Kaufman et al. 1999; Le Petit et al. 2006), and can serve as a discriminant between the "starburst" and "disk" modes of star formation, where the latter is characterized by a larger fraction of diffuse gas (Geach & Papadopoulos 2012).

Here we present new observations of [CI] 1–0 and [CI] 2–1 in a small set of 11 of the brightest gravitationally lensed sub-millimeter galaxies on the sky observed with the *Planck* all-sky survey (Planck Collaboration Int. XXVII 2015; Planck Collaboration Int. XXXIX 2016), *Planck*'s Dusty GEMS. This sample is smaller than those found with other infrared-to-millimeter surveys of high-redshift galaxies (Vieira et al. 2013; Wardlow et al. 2013), which are excellent data sets in their own right, but the GEMS are particularly bright dust continuum emitters, reflecting the high completeness limit of *Planck* at ∼600 mJy.

All GEMS have spectroscopically confirmed redshifts of $z = 2.2-3.6$, and apparent FIR luminosities between 5 and $27 \times 10^{13} \mu L_\odot$ (Cañameras et al. 2015), mainly powered by star formation and boosted by gravitational lensing from foreground clusters or massive individual galaxies by luminosity-averaged factors, $\mu \sim 10-30$ (Cañameras et al. 2017a, 2018a,b, C18 hereafter). Environments probed by these galaxies range from intense, maximally star-forming clumps (Cañameras et al. 2017b, 2018b) to diffuse gas probed by [CII] absorption (Nesvadba et al. 2016), as observed with ALMA and IRAM interferometry. Contamination from AGNs is very weak, contributing ≤10% (Cañameras et al. 2015) of the IR luminosity.

The data we present here were obtained as part of several observing runs with EMIR at the 30-m telescope of IRAM, with the goal of constraining the global gas properties of these galaxies using several CO transitions and the two [CI] lines. In total, we observed 48 CO lines and 15 [CI] lines in 11 galaxies. The results of the analysis of the CO lines, and of detailed radiative transfer and photodissociation region (PDR) models of the CO and [CI] lines, are presented in a companion paper (C18). Here we mainly focus on the physical and empirical properties that can be derived analytically and from [CI] alone, or that use [CI] for empirical constraints.

This paper is organized as follows. In Sect. 2 we present the details of our [CI] observations and data reduction. In Sect. 3 we describe our analysis and how we corrected for gravitational lensing, including the possibility of differential lensing between gas and dust, which we constrain explicitly using sub-arcsecond interferometry. In Sect. 4 we use the [CI] lines to constrain the contribution of atomic carbon to line cooling in order to investigate the heating mechanism, [CI] excitation temperatures, optical depths, abundances, and masses of atomic carbon. We also determine the gas distribution and starburst mode from the [CI] line fluxes and line ratios. In Sect. 5 we discuss the implications of our analysis for H_2 gas mass estimates and the CO-to-H_2 conversion factor. We summarize our results in Sect. 6.

Throughout the paper, we adopt the flat ΛCDM cosmology from Planck Collaboration XVI (2014), with $H_0 = 68\,\mathrm{km\,s^{-1}\,Mpc^{-1}}$, $\Omega_\mathrm{m} = 0.31$, and $\Omega_\Lambda = 1-\Omega_\mathrm{m}$. For example, at $z = 3.0$ this implies a luminosity distance of 26.0 Gpc, and a projected physical scale of 7.9 kpc arcsec^{-1}.

2. Observations and data reduction

We obtained deep spectroscopy of several bright millimeter emission lines, including the [CI] lines presented here, with the wide-band millimeter receiver EMIR at the 30-m telescope of IRAM in several runs between November 2012 and February 2015. In total, we obtained between 81 and 171 min of on-source observing time per source. Individual observing dates and integration times, tuning frequencies, and rms noise values are given in Table 1 for each source and emission line. The analysis of the CO lines is presented in C18.

Depending on the redshift of each source, the [CI] 1–0 line either falls into the 3 mm or 2 mm band, and the [CI] 2–1 line either into the 2 mm or the 1.3 mm band. In two sources, PLCK_G113.7+61.0 and PLCK_G138.6+62.0, the [CI] 1–0 line was used to confirm the spectroscopic redshift previously estimated from a blind line search in the 3 mm band (Cañameras et al. 2015). In most cases, the [CI] lines were observed with dual-band observations, that is, in parallel to other bright millimeter emission lines.

Data were taken under a range of atmospheric conditions. For the 3 mm observations, precipitable water vapor columns (pwv) were mostly between 1 mm and 8 mm. A small part of the observing time suffered from even higher pwv; including these scans did not improve the signal-to-noise ratios (S/Ns) in the final combined data sets, and so these scans were discarded. Observations at 1.3 mm were carried out when the pwv was 1 mm or less.

We used the FTS and WILMA backends with Wobbler switching throws of 60″, which is significantly larger than the diameter of our most extended sources, about 10″. To point the telescope we used blind offsets from radio-loud quasars at distances of a few degrees from our targets. We performed a pointing approximately once every 2 h, and refocused the telescope every 3–4 h, and at sunrise and sunset. Individual scans were 30 s in duration, and we obtained a calibration after every 6 min of observing. The FTS and WILMA backends have intrinsic
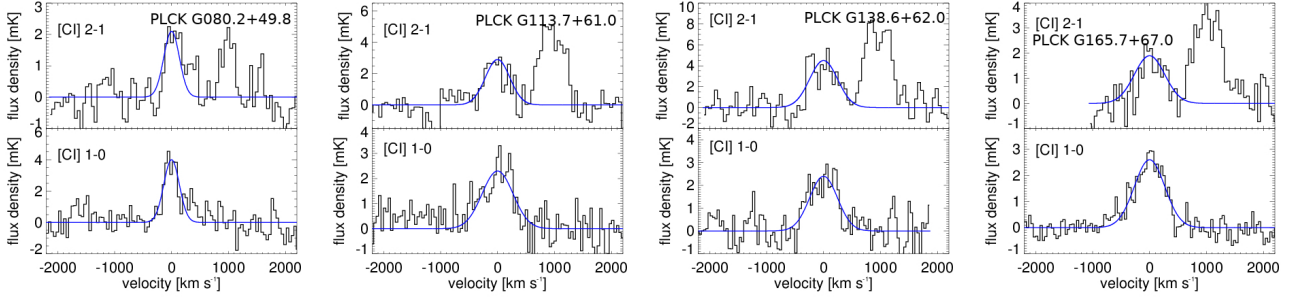
Table 1. Targets and details of our [CI] observations.

Source	RA (J2000)	Dec (J2000)	Redshift	$D_{\rm L}$ (Gpc)	$\mu_{\rm gas} L_{\rm FIR}$ ($10^{13} L_\odot$)	Trans.	ν_0 (GHz)	Date (mm/dd/yy)	ToT (min)	rms (mK)
PLCK_G045.1+61.1	15:02:36.04	+29:20:51	3.43	29.86	8.4 ± 0.1	1–0	111.035	02/03/14	81	1.17
PLCK_G045.1+61.1						2–1	. . .	. . .	. . .	. . .
PLCK_G080.2+49.8	15:44:32.40	+50:23:46	2.60	21.79	4.6 ± 0.1	1–0	136.749	02/03/14	122	2.35
PLCK_G080.2+49.8						2–1	224.400	02/03/14	162	0.82
PLCK_G092.5+42.9	16:09:17.76	+60:45:21	3.26	28.61	24.8 ± 02	1–0	115.639	04/19/14 & 23/02/15	314	1.25
PLCK_G092.5+42.9						2–1	. . .	. . .	. . .	. . .
PLCK_G102.1+53.6	14:29:17.98	+51:29:09	2.92	24.99	7.9 ± 0.1	1–0	. . .	. . .	. . .	. . .
PLCK_G102.1+53.6						2–1	206.267	02/19,21,23/15	81	0.5
PLCK_G113.7+61.0	13:23:02.88	+55:36:01	2.41	19.88	9.9 ± 0.2	1–0	144.160	02/21/15	202	0.3
PLCK_G113.7+61.0						2–1	236.666	02/19/15	150	1.2
PLCK_G138.6+62.0	12:02:07.68	+53:34:40	2.44	20.20	9.0 ± 0.1	1–0	143.677	07/06/13	80	0.8
PLCK_G138.6+62.0						2–1	231.300	02/19/15	102	2.0
PLCK_G145.2+50.9	10:53:2.56	+60:51:49	3.55	31.76	21.8 ± 0.2	1–0	108.167	05/06/14	120	1.3
PLCK_G145.2+50.9						2–1	. . .	. . .	. . .	. . .
PLCK_G165.7+67.0	11:27:14.60	+42:28:25	2.24	18.18	10.3 ± 0.1	1–0	152.070	01/31/14,02/01-04/14	172	0.4
PLCK_G165.7+67.0						2–1	245.500	02/19-20/15	126	0.7
PLCK_G200.6+46.1	09:32:23.67	+27:25:00	2.97	25.14	5.7 ± 0.1	1–0	. . .	. . .	. . .	. . .
PLCK_G200.6+46.1						2–1	206.276	02/21/15	162	1.3
PLCK_G231.3+72.2	11:39:21.60	+20:24:53	2.86	24.00	7.5 ± 0.1	1–0	. . .	. . .	. . .	. . .
PLCK_G231.3+72.2						2–1	209.100	02/20/15	120	0.911
PLCK_G244.8+54.9	10:53:53.04	+05:56:21	3.01	25.47	26.5 ± 0.2	1–0	. . .	. . .	. . .	. . .
PLCK_G244.8+54.9						2–1	205.200	02/19/15	120	2.08

Notes. We list the source name, right ascension and declination, redshift, luminosity distance, observed FIR luminosity, transition, tuning frequency, date of our observations, time spent on the target, and root mean square of the resulting spectrum. Dots indicate lines outside of the atmospheric windows.

resolutions of 0.195 and 2 MHz, respectively, and 16 GHz and 8 GHz of bandwidth, respectively, with horizontal and vertical polarizations observed in parallel. We typically rebinned the data to more appropriate spectral resolutions between 30 and 50 km s^{-1} (see Figs. 2 and 3).

All data were calibrated at the telescope and reduced with the CLASS package of the GILDAS software of IRAM (Gildas Team 2013). We inspected all individual scans by eye and used simple first-order polynomials to correct the baselines, after carefully masking the spectral range expected to be covered by the bright emission lines. For scans with strong "platforming" in their FTS spectra, we used the routine FtsPlatformingCorrection5.class kindly provided by C. Kramer to obtain individual spectral scans with reasonably flat baselines. We used the values given on the EMIR website[1] to approximate the antennae efficiency and to translate the measured brightness temperatures into flux density units (Jy).

3. Line measurements

We detected all targeted [CI] 1–0 and [CI] 2–1 lines, that is, all [CI] lines from galaxies in this sample that fall into the atmospheric windows, with line fluxes between 3.4 and 21 Jy km s^{-1} and FWHM line widths between 220 and 640 km s^{-1}. We used the CLASS function LINE for an initial line fit after subtracting the baseline (Gildas Team 2013), which we then confirmed with the MPFIT routine using IDL (Markwardt 2009). Within the limits imposed by different S/Ns, our fit results are consistent with those obtained for CO by C18.

We followed Solomon & Vanden Bout (2005), for example, to calculate emission-line luminosities, $L_{\rm line}$ and $L'_{\rm line}$, from these fluxes by setting

$$L_{\rm line} = 1.04 \times 10^{-3} \, S_{\rm line} \, \Delta v \, \nu_{\rm rest} \, (1 + z)^{-1} \, D_{\rm L}^2, \tag{1}$$

where $S_{\rm line}\Delta v$ is the velocity-integrated line flux given in Jy km s^{-1}, $\nu_{\rm rest}$ the frequency in the rest-frame in GHz, z is the redshift, $D_{\rm L}$ is the luminosity distance in megaparsecs, and $L_{\rm line}$ is given in solar luminosities. An alternative way to express line luminosities is by setting

$$L'_{\rm line} = 3.26 \times 10^7 \, S_{\rm line}\Delta v \, \nu_{\rm obs}^{-2} \, D_L^2 \, (1 + z)^{-3}, \tag{2}$$

where $\nu_{\rm obs}$ is the observed frequency. The resulting luminosities, L', are proportional to the brightness temperature and are used, for example, to calculate gas masses. L' is given in K km s^{-1} pc^2.

In total, we measured [CI] 1–0 in seven galaxies, and [CI] 2–1 in eight. This includes four galaxies where we measured both [CI] lines (Fig. 1). Individual line profiles are shown in Fig. 2 for [CI] 1–0 and in Fig. 3 for [CI] 2–1. CO(7–6) has a rest frequency of 806.6518 GHz, only 2.7 GHz (or about 1000 km s^{-1}) to the red from the [CI] 2–1 line at 809.3435 GHz. The figures showing the [CI] 2–1 lines therefore also cover the CO(7–6) line in all cases except one. In PLCK_G244.8+54.9, [CI] 2–1 falls right at the band edge; it can be measured with a reliable calibration, unlike CO(7–6). We refer to C18 for a detailed discussion of the line properties of CO(7–6) and other CO lines.

The line profiles are generally smooth enough to be well fitted with single Gaussian profiles (Figs. 1–3). In three of the four galaxies where both [CI] 1–0 and [CI] 2–1 had been measured, the profiles of both lines are similar within the S/N of the present data, and the line centers are at similar redshifts for both transitions (see Fig. 1). In the fourth, PLCK_G113.7+61.0, [CI]1–0, and [CI]2–1 are offset by 700 km s^{-1}, comparable to the FWHM of the [CI] 1–0 line (639 ± 100, Table 2), and perhaps indicating velocity structure within the galaxy. In PLCK_G045.1+61.1, PLCK_G092.5+42.9, and PLCK_G244.8+54.9, the S/Ns are not high enough to fit two separate line components, as done for

---

[1] http://www.iram.es/IRAMES/mainWiki/Iram30mEfficiencies

Fig. 1. [CI] 2–1 and CO(7–6) (*top panel*) and [CI] 1–0 (*bottom panel*) spectra of the four GEMS for which we observed both lines. The blue curve shows the single-component Gaussian fit to the [CI] lines. *Upper panel*: CO(7–6), which is redshifted relative to [CI] 2–1, and is discussed in detail in C18.
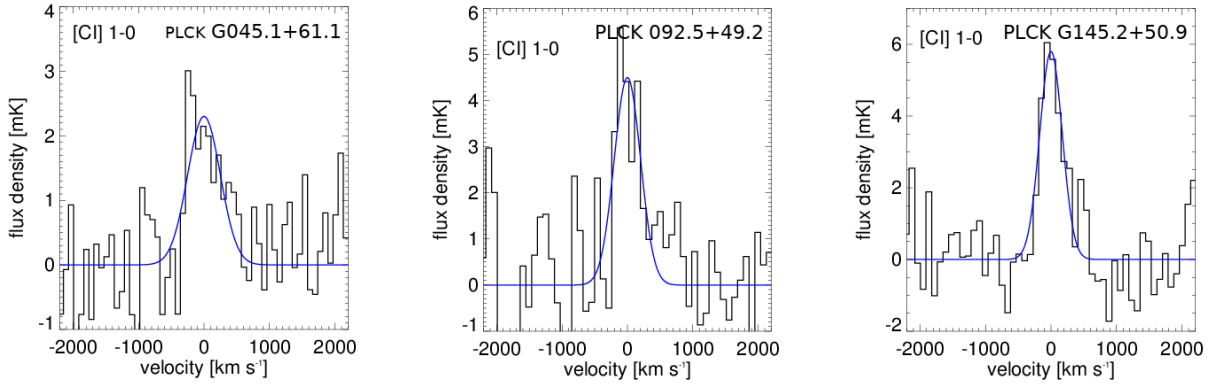

Fig. 2. [CI] 1–0 line of the GEMS for which [CI] 2–1 and CO(7–6) fall outside the atmospheric windows. Blue curves indicate the single-component Gaussian fits to the [CI] 1–0 line.

the brightest CO lines (C18). The results of our line fits are listed in Table 2, and are not corrected for gravitational lensing. Luminosity-weighted magnification factors are given in Table 1 of C18.

We constructed detailed gravitational lens models for all GEMS (Cañameras et al. 2017a, 2018b, and in prep.), which we derived with the publicly available LENSTOOL package (Jullo & Kneib 2009). LENSTOOL models the lensing potentials as pseudo-isothermal ellipsoids and derives the properties of these ellipsoids by calculating the expected position of multiple gravitationally lensed arclets behind the lensing structure. We used the HST/WFC3 imaging recently presented by Frye et al. (2019), for the five sources where it was available, and ground-based CFHT imaging with 0.8″–1.0″ resolution otherwise. Residuals between observed and modeled positions of arclets are smaller than the size of the PSF in all models.

From the detailed lensing models (constrained from the WFC3 morphologies), sub-arcsecond millimeter dust, CO emission-line maps, and the kinematic properties of the gas in each source (thereby taking into account the source morphology and differential lensing), we calculate luminosity-weighted average magnification factors separately for the gas and the dust, finding values between 6 and 30 (see Table 1 of C18). Deriving average magnifications for the dust and gas from pixel-by-pixel reconstructions of the source-plane image suggests uncertainties from differential lensing of about 25%.

PLCK_G138.6+62.0 is the only galaxy for which we do not have spatially resolved millimeter or sub-millimeter morphologies, so we adopt an empirically estimated factor $\mu = 20$ in this case (for details see Cañameras et al. 2015). For the [CI] line we are most concerned with here, we use the magnifica-

tion factors derived from the CO line emission, i.e., assuming that both CO and [CI] come from gas clouds with similar spatial distributions. We thus neglect a potential contribution from faint, very extended diffuse gas outside the bright star-forming regions themselves. This assumption can be tested indirectly by comparing the line profiles, which indeed do not show significant differences when integrated over entire sources. The values we used for this paper are listed in Table 3.

We can also use the different estimates for the dust and gas masses to roughly constrain the impact of differential lensing on the various lines in the sub-millimeter and millimeter regimes, finding rather moderate typical differences of about 25%, without any dramatic outliers. This is also to be expected, given that the dust and the mid-J CO and [CI] 2–1 lines should mainly originate from gas and dust in actively star-forming regions (Cañameras et al. 2015, and noting that the GEMS do not show evidence of luminous AGNs).

We can also constrain the likely impact of differential lensing directly from the present data. As we show in Sect. 4.1, the cooling budget from [CI] relative to the FIR luminosity and to CO(4–3) is within a factor of two of that found in other samples of nearby and high-redshift galaxies, including gravitationally lensed and unlensed galaxies (Figs. 4 and 5), respectively. In the absence of a systematic conspiracy with other astrophysical quantities, this suggests that differential lensing does not introduce larger uncertainties than other effects. Moreover, integrated mass estimates from CO(1–0) and [CI] 1–0 are very similar, as we show in Sect. 5.

For the same reason, we consider it unlikely that we have missed a dominant component of CO-dark, [CI] 1–0 -emitting gas that is strongly gravitationally lensed and has significant
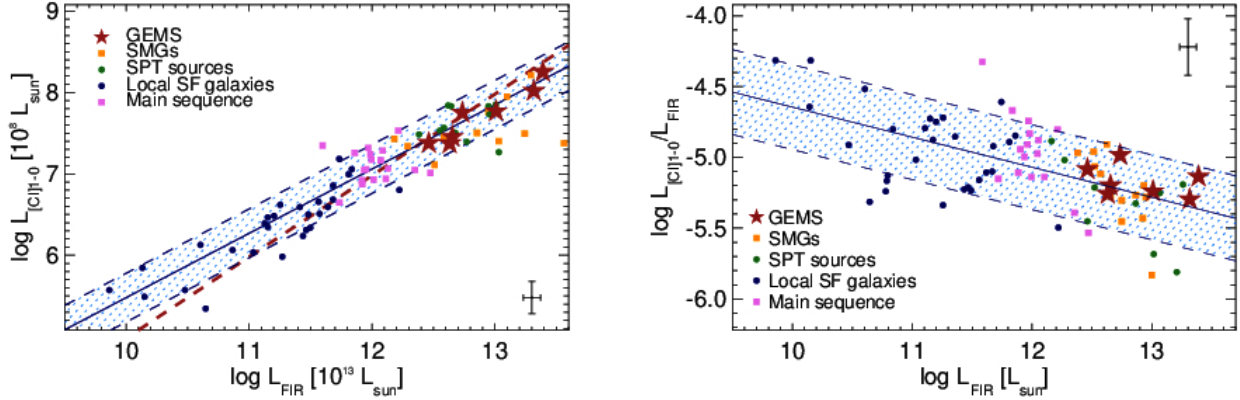
Fig. 3. [CI] 2–1 and CO(7–6) lines of the GEMS for which [CI] 1–0 falls outside the atmospheric windows. For PLCK_G244.8+54.9, [CI] 2–1 falls right at the edge of the band, so that [CI] 2–1 can be reliably measured, but CO(7–6) cannot. Blue curves indicate the single-component Gaussian fits to the [CI] 2–1 line.

Table 2. [CI] line properties.

Source	Line	ν_{obs} (GHz)	Redshift	$FWHM$ (km s^{-1})	μT_K (mK)	$\mu I_{[CI]}$ (Jy km s^{-1})	$\mu L'$ (10^{11} K km s^{-1} pc^2)	μL ($10^8 L_\odot$)
PLCK_G045.1+61.1	[CI] 1–0	111.133 ± 0.024	3.4280 ± 0.0002	589 ± 145	2.3	8.4 ± 1.7	2.3 ± 0.5	8.6 ± 1.7
PLCK_G080.2+49.8	[CI] 1–0	136.767 ± 0.008	2.5985 ± 0.0002	242 ± 61	3.8	6.2 ± 0.9	1.1 ± 0.2	4.0 ± 0.7
PLCK_G080.2+49.8	[CI] 2–1	224.847 ± 0.025	2.5995 ± 0.0003	312 ± 24	2.3	5.8 ± 1.0	0.37 ± 0.08	6.2 ± 1.2
PLCK_G092.5+42.9	[CI] 1–0	115.641 ± 0.016	3.2559 ± 0.0006	475 ± 128	4.5	13.5 ± 2.6	3.3 ± 0.6	12.8 ± 2
PLCK_G102.1+53.6	[CI] 2–1	206.608 ± 0.006	2.9173 ± 0.0001	220 ± 21	2.3	4.0 ± 0.4	0.3 ± 0.3	5.2 ± 0.5
PLCK_G113.7+61.0	[CI] 1–0	144.019 ± 0.020	2.41730 ± 0.0003	639 ± 100	2.3	10.2 ± 1.2	1.5 ± 0.2	5.9 ± 0.7
PLCK_G113.7+61.0	[CI] 2–1	237.395 ± 0.002	2.40927 ± 0.0001	504 ± 10	2.9	9.2 ± 1.0	0.5 ± 0.05	8.6 ± 0.9
PLCK_G138.6+62.0	[CI] 1–0	142.974 ± 0.020	2.4423 ± 0.0003	575 ± 86	2.4	9.5 ± 1.5	1.5 ± 0.2	5.6 ± 0.9
PLCK_G138.6+62.0	[CI] 2–1	235.129 ± 0.003	2.4421 ± 0.0001	526 ± 5	4.5	18.8 ± 0.2	1.1 ± 0.01	18.0 ± 0.1
PLCK_G145.2+50.9	[CI] 1–0	108.204 ± 0.009	3.5485 ± 0.0003	405 ± 63	5.8	14.8 ± 3.5	4.2 ± 1.0	16.0 ± 3.8
PLCK_G165.7+67.0	[CI] 1–0	152.079 ± 0.009	2.2362 ± 0.0001	629 ± 46	2.6	11.1 ± 2.8	1.5 ± 0.4	5.6 ± 1.4
PLCK_G165.7+67.0	[CI] 2–1	250.059 ± 0.025	2.2366 ± 0.0002	418 ± 6	2.6	8.3 ± 0.2	0.4 ± 0.09	6.8 ± 0.1
PLCK_G200.6+46.1	[CI] 2–1	203.697 ± 0.018	2.97326 ± 0.0001	412 ± 5	2.5	8.3 ± 0.1	0.7 ± 0.01	11.1 ± 0.1
PLCK_G231.3+72.2	[CI] 2–1	209.729 ± 0.015	2.85899 ± 0.0001	319 ± 18	2.7	6.9 ± 0.4	0.5 ± 0.03	8.7 ± 0.5
PLCK_G244.8+54.9	[CI] 2–1	202.113 ± 0.002	3.00440 ± 0.0001	586 ± 5	4.5	21.0 ± 0.2	1.7 ± 0.02	28.6 ± 0.3

Notes. We list the source name, the line, observed frequency, redshift, full-width at half maximum of the line, main-beam brightness temperature, integrated line flux, and the line luminosity in units proportional to brightness temperature and energy, respectively. We give observed values here, where μ indicates the gravitational magnification factor. Luminosity-weighted average gravitational correction factors are given in Table 1 of C18, and are repeated in our Table 3 for convenience.

transversal positional or velocity offsets from the molecular clouds. However, this does not imply that CO and [CI] are exactly co-spatial (e.g., Offner et al. 2014). On scales of a few hundred parsecs or less, smaller than the area that is being magnified by the gravitational lens, and in directions roughly along the line of sight, or perpendicular to the magnification direction, the diffuse and dense gas may or may not be well mixed, without impact on differential lensing. This would be the case for a clumpy interstellar medium for example. Sizes of the order of 100 pc are consistent with the Jeans-length, for example, in dense fragmenting gas disks of high-*z* galaxies including the GEMS (Hodge et al. 2018; Cañameras et al. 2017b; Swinbank et al. 2011, C18).

4. [CI] diagnostic properties

With the line fluxes measured in Sect. 3, we can derive luminosity ratios between the [CI] 2–1 and [CI] 1–0 lines for the four galaxies, in cases where both lines have been measured. We find ratios of $L_{CI2-1/CI1-0} = 1.2$–3.3 (Table 2). Given the wide range in gas conditions probed by the [CI] lines, their ratios with each

other, with other emission lines (in particular CO), and with the FIR continuum, all provide interesting diagnostic constraints.

A thorough analysis of the gas excitation using the radiative transfer code RADEX and PDR model of Kaufman et al. (1999) has already been presented by C18, using [CI] as well as multiple CO lines, generally between $J = 3-2$ and $J = 7-6$, and even above $J = 9-8$ for two galaxies. These latter authors find that the gas in the GEMS is characterized by luminosity-weighted average gas densities of $n \sim 10^{4-5}$ cm^{-3}, and radiation fields of 10^{2-4} G_0; these are in the range of other starburst galaxies at low and high redshift. Here we complement and extend these analyses by focusing on the constraints that can be derived solely from the atomic carbon lines, as well as several empirical constraints on the gas masses and the distribution of interstellar gas in the GEMS.

4.1. Atomic line cooling

We can use the [CI] line luminosities, L_{CI}, and the FIR luminosities from Cañameras et al. (2015) integrated over a wavelength range of $8-1000\,\mu$m to estimate the total cooling from atomic gas in the GEMS. Using the luminosities $L_{[CI1-0]}$ and $L_{[CI]2-1}$

Fig. 4. Cooling budget through [CI]1–0 line emission. [CI]1–0 luminosity (*left panel*), L_{CI1-0}, and ratio with FIR luminosity, L_{CI1-0}/L_{FIR} (*right panel*), as a function of FIR luminosity, L_{FIR}. The red stars are the GEMS. Blue, pink, green, and yellow symbols indicate the samples of low-redshift spiral galaxies from Kamenetzky et al. (2016), the main sequence galaxies at $z \sim 1.2$ from Valentino et al. (2018), the high-redshift samples of gravitationally lensed sources from the South Pole Telescope (Bothwell et al. 2017) and the submillimeter galaxies of Alaghband-Zadeh et al. (2013), respectively. The blue line shows the average relationships derived by Valentino et al. (2018) for their main sequence galaxies and comparison samples, and the red line shows an equivalent relationship with a slope of unity. Blue hatched bands show a range of ±2 around these averages. Typical error bars of our measurements are shown in the lower- and upper-right corners of the two panels, respectively.

listed in Table 2, we find L_{CI1-0}/L_{FIR} and L_{CI2-1}/L_{FIR} ratios of 5 to 20×10^{-6}. We adopted the measured values and did not correct for differences in dust and gas magnifications, which would have changed our results by at most about 25%. Values for individual galaxies are given in Table 6.

Bothwell et al. (2017) found $L_{CI1-0}/L_{FIR} = 7.7 \pm 2.4 \times 10^{-6}$ in their sample of 13 gravitationally lensed galaxies at $z \sim 4$ from the SPT survey. Walter et al. (2011) measured $L_{CI1-0}/L_{FIR} = 1-15 \times 10^{-6}$, albeit using FIR luminosities that were derived prior to the launch of the *Herschel* satellite, from the flux density at 850 μm and a fiducial dust temperature of $T = 35$ K. Alaghband-Zadeh et al. (2013) found $L_{CI1-0}/L_{FIR} = 2.6 \pm 0.5 \times 10^{-5}$ for their newly observed sources, and $L_{CI1-0}/L_{FIR} = 8 \times 10^{-6}$ for sources culled from the literature (which have considerable overlap with the sample of Walter et al. 2011). Valentino et al. (2018) find about half the value, $L_{[CI]1-0}/L_{FIR} = 1.4 \times 10^{-5}$ for a set of main sequence galaxies at $z = 1.2$. The GEMS therefore fall within the wide range previously found in other high-redshift galaxies. This can also be seen from Fig. 4, where we plot L_{CI} and L_{CI}/L_{FIR} as a function of L_{FIR}. The GEMS follow similar trends to the samples of low- and high-redshift galaxies. All fall within a factor of two of the best-fit relations.

In nearby ULIRGs, Rosenberg et al. (2015) find that the combined ratio of the two [CI] lines is $L_{CI10+21}/L_{FIR} = 1 - 5 \times 10^{-5}$ in most galaxies, except for the lowest FIR luminosities in the LIRG regime, where ratios can reach about 1×10^{-4}. The GEMS for which both lines have been measured have combined ratios $L_{CI10+21}/L_{FIR} = 1.2$ and 2.6×10^{-5}, which are in the lower range found in the nearby universe; we find similar values when using the [CI] 2–1 / [CI] 1–0 ratios of the GEMS as a fiducial correction factor of the missing second line in the samples of Bothwell et al. (2017) and Alaghband-Zadeh et al. (2013). Riechers et al. (2013) found $L_{CI10+21}/L_{FIR} = 2 - 5 \times 10^{-5}$ in a luminous starburst at $z = 6.3$.

This suggests, at least for the small sample sizes and S/Ns obtained for current samples of high-redshift galaxies, that the contribution of atomic gas to the overall cooling budget of the galaxies has remained approximately constant since about 1 Gyr after the Big Bang, and has at most slightly increased with cosmic time. In nearby galaxies, the two [CI] lines contribute together about 1.5% to the total gas cooling rate (Rosenberg et al. 2015).
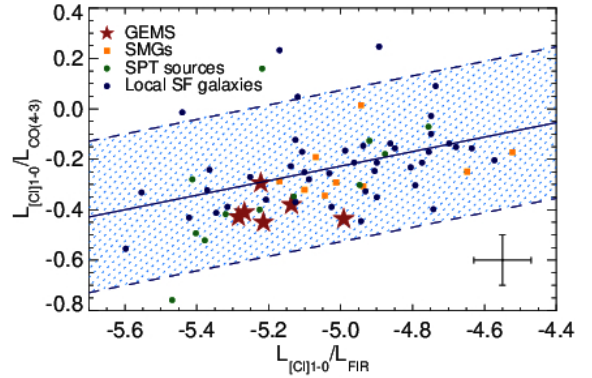

Fig. 5. Ratio of L_{CI1-0} to $L_{CO(4-3)}$ as a function of the cooling budget through [CI] 1–0. The red stars are the GEMS. Blue, green, and orange dots indicate the samples of low-redshift star-forming galaxies from Kamenetzky et al. (2016), and the high-redshift samples of gravitationally lensed sources from the SPT (Bothwell et al. 2017) and the submillimeter galaxies of Alaghband-Zadeh et al. (2013), respectively. The blue line shows the average relationship derived from the comparison samples. The blue hatched region shows a range of a factor of ±2 around this average. The typical measurement uncertainty is shown in the lower-right corner.

Finding similar line-to-continuum flux ratios in high- and low-redshift galaxies imposes at least loose upper limits on the importance of global changes in the gas-heating processes in high-redshift galaxies due to cosmic rays (Bisbas et al. 2017) or X-rays (Meijerink et al. 2007). If, on top of the heating from UV photons, bolometrically significant additional heating mechanisms like X-rays, cosmic rays, or shocks were present (which predominantly boost the line, but not the continuum luminosities at long wavelengths), we would expect these ratios to be systematically greater in high-redshift galaxies. Our results suggest that this is not the case. Given the scatter in the relationships, however, this does not imply that such mechanisms are not present; they simply cannot dominate the overall gas heating budgets.

4.2. Heating mechanism and AGN contamination

The ratio of the [CI] 2–1 and the [CI] 1–0 line fluxes can inform us about the presence of X-ray heating from AGNs.

Radiative-transfer models of gas heating from UV photons imply an upper limit to the [CI] 2–1/[CI] 1–0 ratio, which cannot be exceeded without the presence of a harder incident radiation field like that from an AGN. Meijerink et al. (2007) calculated line ratios for gas heated by UV and X-ray photons, as expected for regions of intense star formation and circum-nuclear environments within AGN host galaxies, respectively. For a wide range in gas density between about 10 and 10^6 cm^{-3}, they predict that X-ray heating will produce line ratios between [CI] 2–1 and [CI] 1–0 of $L_{21}/L_{10} \gtrsim 3.5$. Ratios lower than this are a clear indication of UV heating in gas with typical densities of a few times 10^{2-4} cm^{-3} as in the GEMS (C18).

In Table 4 we give the luminosity ratios for the four galaxies where we measured both [CI] lines. In PLCK_G080.2+49.8, PLCK_G113.7+61.0, and PLCK_G165.7+67.0 we find very similar ratios of between $L_{[CI2]}/L_{CI10} = 1.2 \pm 0.3$ and $L_{CI21}/L_{CI10} = 1.5 \pm 0.2$. However, the ratio in the fourth source, PLCK_G138.6+62.0, is significantly higher: $L_{CI21}/L_{CI10} = 3.3 \pm 0.1$. This source therefore falls near the regime where an AGN could have an impact, although it is still within the range expected for intensely star-forming systems. Finding little evidence for AGN X-ray heating from the line ratios confirms our previous results from the mid-to-far-infrared spectral energy distributions, which also suggest that AGNs are weak compared to the UV radiation from young stellar populations (Cañameras et al. 2015), or absent.

4.3. Star-formation mode

Greve et al. (2012) and Papadopoulos & Geach (2012) proposed that the ratio of the line luminosities of CO(4–3) and [CI] 1–0 can be used to qualitatively infer the relative amount of dense molecular and more diffuse gas. They associate higher ratios of dense molecular to diffuse gas with starburst galaxies, and galaxies with a more balanced ratio of dense and diffuse gas with quiescently star-forming (disk-like) galaxies. From observations of nearby galaxies, they infer an average ratio of $r_{CO(4-3)/CI10} = 4.55 \pm 1.5$ for starburst (ULIRG) environments, and $r_{CO(4-3)/CI10} = 0.45 - 1.3$ for disk galaxies. In the GEMS, the corresponding ratios are between 2.6 and 5.8. For galaxies where we have a direct measurement of [CI] 1–0, we find ratios of $2.9-3.3$, and $2.6-5.8$ for the galaxies without [CI] 1–0 measurements (where we used the [CI] 2–1 measurement corrected for an average [CI] 2–1/[CI] 1–0 ratio instead). These results are all in the starburst regime, as also expected from the high star-formation rate densities found by Cañameras et al. (2017b).

We note that using [CI] 2–1 instead of [CI] 1–0 can lead to uncertainties of factors of two to three, and additionally for some galaxies we used CO(3–2) instead of CO(4–3) because the latter falls outside the atmospheric window (see Table 5). From the CO spectral line energy diagrams shown by C18, we know that this might bias the line ratios of the GEMS about 25% low compared to estimates with CO(4–3). Since we only aim at loosely classifying the GEMS between two groups that differ by an order of magnitude on average, and do not use the precise value of these line ratios, we find that our conclusions are not compromised by these additional systematic uncertainties.

4.4. Excitation temperatures and optical depth

One of the main advantages in using [CI] instead of CO lines as a tracer of mass is that they should remain optically thin out to the high volume-averaged column densities typically encountered in rapidly star-forming dusty high-redshift galaxies (e.g.,

Table 3. Intrinsic masses of atomic carbon, M_{CI}, and molecular gas, M_{H_2}, estimated from [CI] 1–0 in the seven galaxies where we observed this line.

Source	M_{CI} $(10^7 \, M_\odot)$	M_{H_2} $(10^{10} \, M_\odot)$	μ_{gas}
PLCK_G045.1+61.1	1.9	13.5	15.5
PLCK_G080.2+49.8	0.8	6.2	15.9
PLCK_G092.5+42.9	3.7	25.8	12.0
PLCK_G113.7+61.0	2.0	14.6	9.7
PLCK_G138.6+62.0	1.0	6.8	20.
PLCK_G145.2+50.9	6.3	43.7	8.9
PLCK_G165.7+67.0	0.8	5.8	24.1

Notes. For convenience, we also list the magnification factors for the gas, μ_{gas}, taken from Table 1 of C18, which we have used to correct these measurements for gravitational lensing.

Walter et al. 2011). In other words, the line luminosity remains proportional to the total mass. Since we have both the [CI] 2–1 and [CI] 1–0 line measured in four GEMS, we can test this assumption directly.

We saw in Sect. 4.2 that the gas in the present galaxies is predominantly heated by UV photons and we can therefore follow Schneider et al. (2003) and Walter et al. (2011) who derived the optical depth, τ, of the [CI] 1–0 emitting gas in PDRs by setting

$$\tau_{[CI]1-0} = -\ln\left(1 - T_{mb,[CI]1-0} \, (e^{23.6/T_{ex}} - 1)/23.6\right). \quad (3)$$

Here T_{ex} is the excitation temperature of the gas in kelvin, K, assuming LTE, and T_{mb} is the rest-frame peak intensity of the line in main beam brightness temperature, and is also given in kelvin. A similar expression can be given for [CI] 2–1:

$$\tau_{[CI]2-1} = -\ln\left(1 - T_{mb,[CI]2-1} \, (e^{38.8/T_{ex}} - 1)/38.8\right). \quad (4)$$

The excitation temperature in kelvin can be found from the ratio of line luminosities, L'_{CI2-1}/L'_{CI1-0}, by setting

$$T_{ex} = h\nu_{21}/k_B \, \ln\left(\frac{N_{10}}{N_{21}} \frac{g_{21}}{g_{10}}\right)^{-1} = \frac{38.8}{\ln(2.11/R)} \, [K], \quad (5)$$

where R is the ratio between the integrated luminosities, L', of the [CI] 2–1 and [CI] 1–0 lines, k_B is the Boltzmann constant, h is Planck's constant, ν_{21} the rest-frame frequency of the [CI] 2–1 line, N_{10} and N_{21} are the column densities of the [CI] 1–0 and 2–1 lines, respectively, and g_{21} and g_{10} are the corresponding Gaunt factors.

With the luminosities and main-beam brightness temperatures given in Table 2, we find excitation temperatures, $T_{ex} = 21-37$ K. This is consistent with previous work (Jiao et al. 2017) and systematically lower than the dust temperatures found by Cañameras et al. (2015), which are between 33 and 50 K for the same galaxies; this might indicate that [CI] has a significant extended component (see also Sect. 5), or that the dust and atomic gas are not in thermal equilibrium.

Both lines are optically thin in the GEMS, and comparable to those in other high-redshift galaxies (Walter et al. 2011; Alaghband-Zadeh et al. 2013). The corresponding optical depths of the [CI] 1–0 line are between $\tau_{10} = 0.01$ and 0.14, and for the [CI] 2–1 line are generally between $\tau_{21} = 0.01$ and 0.06. In PLCK_G244.8+54.9 we find $\tau_{21} = 0.55$ for a fiducial temperature of $T_{ex} = 20$ K. This temperature is likely too low for a galaxy with such highly excited gas (C18). For $T_{ex} = 40$ K, we would find a more typical value of $\tau_{21} = 0.13$. Results for individual galaxies are listed in Table 4; in galaxies where only one

Table 4. Ratios of line luminosities to the FIR luminosity of [CI] 1–0 and [CI] 2–1, and luminosity ratios of [CI] 2–1 and [CI] 1–0.

Source	L_{CI10}/L_{FIR} $(\times 10^{-6})$	L_{CI21}/L_{FIR} $(\times 10^{-6})$	L_{CI21}/L_{CI10}	L'_{CI21}/L'_{CI10}	T_{ex} (K)	τ_{CI1-0}	τ_{CI2-1}	μM_{CI} $(10^8 M_\odot)$
PLCK_G045.1+61.1	10.2 ± 2.0	. . .	. . .	. . .	20^a	0.04^a	. . .	3.0 ± 0.5
PLCK_G080.2+49.8	8.7 ± 1.5	13.5 ± 2.6	1.6 ± 0.2	0.33 ± 0.1	$22.3^{+3.75}_{-3.5}$	0.14	0.05	1.3 ± 0.3
PLCK_G092.5+42.9	5.2 ± 0.8	. . .	. . .	. . .	20^a	0.07^a	. . .	4.4 ± 0.3
PLCK_G102.1+53.6	. . .	6.6 ± 0.6	. . .	. . .	. . .	. . .	0.02^a	. . .
PLCK_G113.7+61.0	6.0 ± 0.7	8.6 ± 0.9	1.5 ± 0.2	0.33 ± 0.2	$21.0^{+8.7}_{-7.3}$	0.03	0.02	2.0 ± 0.4
PLCK_G138.6+62.0	6.1 ± 1.0	20.0 ± 0.1	3.3 ± 0.1	0.73 ± 0.2	$36.7^{+10.5}_{-8.3}$	0.01	0.01	1.9 ± 0.3
PLCK_G145.2+50.9	7.3 ± 1.7	. . .	. . .	. . .	20^a	0.02^a	. . .	5.6 ± 1.0
PLCK_G165.7+67.0	5.4 ± 1.3	6.6 ± 0.1	1.2 ± 0.3	0.27 ± 0.1	$18.7^{+3.38}_{-3.5}$	0.02	0.01	2.0 ± 0.3
PLCK_G200.6+46.1	. . .	19.5 ± 0.2	. . .	. . .	. . .	. . .	0.01^a	. . .
PLCK_G231.3+72.2	. . .	11.6 ± 0.7	. . .	. . .	. . .	. . .	0.06^a	. . .
PLCK_G244.8+54.9	. . .	10.8 ± 0.1	. . .	. . .	. . .	. . .	0.55^a	. . .

Notes. Excitation temperature and optical depths of [CI] 1–0 and [CI] 2–1 are also given, as well as the mass of atomic carbon (not corrected for gravitational magnification μ) for galaxies with [CI] 1–0 observation. $^{(a)}$For galaxies without either [CI] 1–0 or [CI] 2–1 measurements, we adopted a fiducial excitation temperature of $T_{ex} = 20$ K.

[CI] line falls into the atmospheric windows, we adopt a fiducial excitation temperature of $T_{ex} = 20$ K, consistent with the average of three of the GEMS. Similar temperatures are found for the lower-excitation component traced by CO lines by Yang et al. (2017) and C18. By using the lowest representative temperature measurement, we bias the optical depth of the lines high, since the gas becomes optically thicker with decreasing temperature. Had we adopted $T_{ex} = 37$ K instead (the highest excitation temperature measured amongst the GEMS), we would have obtained optical depths that were approximately 80% lower.

4.5. Mass of atomic carbon and carbon abundances

A major advantage of using optically thin lines for mass estimates is that the line luminosity is proportional to the mass of the tracer. We follow Walter et al. (2011) and Weiß et al. (2005b) in estimating the mass of atomic carbon by setting

$$M_{CI} = 5.71 \times 10^{-4} Q(T_{ex}) 1/5 e^{T_1/T_{ex}} L'_{CI10} [M_\odot], \tag{6}$$

where T_{ex} is the excitation temperature, $Q(T_{ex})$ the partition function $Q(T_{ex}) = 1.0 + 3e^{-T_1/T_{ex}} + 5e^{-T_2/T_{ex}}$, and L'_{CI10} are the measured luminosities of [CI] 1–0.

We use the measured excitation temperature, T_{ex}, for the four galaxies where we observed both [CI] line fluxes (Table 4). The quantities $T_1 = 23.6$ K and $T_2 = 62.5$ K correspond to the energies above the ground state for [CI] 1–0 and [CI] 2–1, respectively. Results are listed in Table 6. Overall, we find that atomic carbon masses are between $8 \times 10^6 M_\odot$ and $5 \times 10^7 M_\odot$ after correcting for the gravitational magnification given in Table 3.

In principle, both lines of [CI] can be used as mass tracers. Weiß et al. (2005b) give an equivalent equation to Eq. (6) for [CI] 2–1. However, in practice, estimates based on [CI] 2–1 are much more sensitive to the excitation temperature. Whereas the mass estimate derived from [CI] 1–0 changes by only about 1% for a temperature range between 20 and 50 K, mass estimates from [CI] 2–1 change by more than a factor of three. Since the excitation temperature in the four galaxies with [CI] 1–0 and [CI] 2–1 measurements does not correlate with the dust temperature, to estimate robust excitation temperatures from [CI] 2–1, we would need to observe both lines, in which case we would estimate the atomic carbon mass directly from [CI] 1–0. We therefore do not

derive carbon mass estimates for the GEMS that have only [CI] 2–1 measurements.

Combining our mass estimates of atomic carbon with the molecular gas mass estimates derived from CO by C18 allows us to estimate a carbon abundance, $X_{CI} = X[CI]/X[H_2] = M_C/6 M_{H_2}$. Obviously, a CO mass estimate must be chosen for this calculation that in itself does not depend on carbon abundance. We are using the ULIRG conversion factor, $\alpha_{CO,ULIRG} = 0.8 M_\odot / [K \, km \, s^{-1} \, pc^2]$, which satisfies this criterion. Solomon et al. (1997) derived this value from dynamical mass estimates of nearby ULIRGs, supposing that the molecular gas mass is equal to the difference between dynamical and stellar mass. For the same reason, $\alpha_{CO,ULIRG}$ also naturally accounts for He.

Using the total molecular gas mass estimates of C18, and assuming, for the sake of this specific analysis, that $\alpha_{CO,ULIRG}$ is the perfect choice for these targets (we discuss this choice more broadly in the following section), we find carbon abundances of between 2.3 and 4.0×10^{-5} (Table 6).

These abundance estimates are consistent with the canonical value proposed by Weiß et al. (2005a), and derived for M82. They are also consistent with previous work by Alaghband-Zadeh et al. (2013) and Danielson et al. (2011) for gravitationally lensed, dusty starburst galaxies at similar redshifts; these authors found values of $3-4 \times 10^{-5}$, comparable to what we find here. Several recent analyses, however, come to different conclusions. For example, Bothwell et al. (2017) found a high average carbon abundance of $X_{CI} = 7.3 \times 10^{-5}$ in a sample of 13 strongly lensed dusty starburst galaxies from the SPT survey at $z \sim 4$, when adopting $\alpha_{CO,ULIRG}$, whereas Valentino et al. (2018) very recently found significantly lower values in a sample of main sequence disk galaxies at $z = 1.2$, adopting a higher CO-to-H_2 conversion factor, which is presumably more appropriate for main sequence galaxies. We continue the discussion of the carbon abundances after deriving molecular gas masses from the [CI] 1–0 luminosities in the following section.

5. Molecular gas mass estimates from [CI] and CO

Weiß et al. (2005b), Papadopoulos et al. (2004), and Wagg et al. (2006) were among the first to propose the use of [CI] emission-line measurements to estimate total molecular gas masses for high-redshift galaxies. The main motivation was that these lines are bright and optically thin, and that for a given carbon

abundance and excitation parameter, Q_{10}, a simple scaling between [CI] 1–0 line flux and total gas mass can be given, as follows:

$$M_{\mathrm{H_2,[CI]}} = 1380 \times \frac{D_{\mathrm{L}}^2}{(1+z)} A_{10,-7}^{-1} X_{\mathrm{CI},-5}^{-1} Q_{10}^{-1} I_{\mathrm{CI}} \; [M_\odot], \qquad (7)$$

where D_{L} is the luminosity distance in units of gigaparsecs, z is redshift, and I_{CI} is the integrated line flux of [CI] 1–0 in Jy km s^{-1}. The Einstein A coefficient for [CI] 1–0, A_{10}, is given in units of 10^{-7} s^{-1}, and the carbon abundance, X_{CI}, is in units of 10^{-5}.

We set $X_{\mathrm{CI}} = 3 \times 10^{-5}$, the standard value that has also been commonly adopted in previous work (e.g., Walter et al. 2011), and $A_{10} = 7.93 \times 10^{-8}$, similar to previous authors. For Q_{10} we adopted 0.49, the median Q_{10} value used by Papadopoulos et al. (2004) and also used previously by Alaghband-Zadeh et al. (2013).

With the flux measurements listed in Table 2, between 3 and 21 Jy km s^{-1}, and the redshifts listed in the same table, we find total molecular gas mass estimates, $M_{\mathrm{H2,CI}}$ between 10 and $40 \times 10^{11} \, \mu^{-1} \, M_\odot$ for the seven galaxies for which [CI] 1–0 has been measured. Results for individual sources are listed in Table 6.

In Table 6, we also compare with molecular gas mass estimates derived from CO line emission, for a CO-to-H$_2$ conversion factor of $\alpha_{\mathrm{CO,ULIRG}} = 0.8 \, M_\odot$ / [K km s^{-1} pc^2]. We follow C18, who derived gas masses from the measured CO(4–3) or CO(3–2) luminosities, depending on which line falls into the atmospheric windows, and taking CO(3–2) when both lines are available. These luminosities, L', were corrected by ratios of $R_{32} = L'_{\mathrm{CO(3-2)}}/L'_{\mathrm{CO(1-0)}} = 0.4$ and $R_{43} = L'_{\mathrm{CO(4-3)}}/L'_{\mathrm{CO(1-0)}} = 0.3$ (C18) to extrapolate to $L'_{\mathrm{CO(1-0)}}$. C18 derived these average line ratios by comparing with the CO(1–0) mass estimates of Harrington et al. (2018), which are available for four GEMS, for $\alpha_{\mathrm{CO,ULIRG}} = 0.8 \, M_\odot$ / [K km s^{-1} pc^2]. In the following we use these ratios to adopt a common procedure for our entire sample, including galaxies with and without CO(1–0) measurements.

With these line ratios, we find excellent agreement between the masses derived from [CI] and CO for all GEMS for which [CI] 1–0 observations are available. Amongst the four sources for which CO(1–0) measurements are available, three have consistent mass estimates from CO(1–0) and [CI] 1–0 within the measurement uncertainties. Only one source, PLCK_113.7+61.1, has a somewhat higher mass estimate from [CI] 1–0 than from CO(1–0), with a ratio $M_{\mathrm{H2,CI10}}/M_{\mathrm{H2,CO10}} = 1.4 \pm 0.1$. For the overall sample, and using molecular gas mass estimates derived from CO(4–3) or CO(3–2), five of seven sources have consistent mass estimates (within 2σ), and two sources have somewhat larger mass estimates from [CI] 1–0 than from CO: $M_{\mathrm{H2,CI10}}/M_{\mathrm{H2,CO10}} = 1.7 \pm 0.2$. Individual results are listed in Table 6.

Finding consistent mass estimates with two independent tracers is certainly an encouraging result, and may serve as a validation of applying low-redshift calibrations to (at least this type of) high-redshift galaxies. This result also confirms that using low, average CO-to-H$_2$ conversion factors akin to the used factor $\alpha_{\mathrm{CO,ULIRG}} = 0.8 \, M_\odot$ / [K km s^{-1} pc^2] (Solomon et al. 1997), average carbon abundance of about $X_{\mathrm{CI}} = 3 \times 10^{-5}$ (Weiß et al. 2005a), and excitation parameter $Q_{10} \sim 0.5$ (Papadopoulos et al. 2004), is an adequate, internally consistent choice of parameters.

However, this result should be interpreted with some caution. In particular, it cannot be used as a justification for any particular choice of X_{CI} or α_{CO}, since both are degenerate, as inserting the expression of carbon abundance explicitly into Eq. (7) immediately shows. Consequently, the largest systematic uncertainty

in carbon abundance measurements, and in molecular gas mass estimates from [CI], is still α_{CO}.

The total atomic carbon mass estimates, however, are independent of the chosen α_{CO}. Therefore, significantly increasing α_{CO} for galaxies like the GEMS would also imply that we should adopt equally low carbon abundances. We argued in C15 that the metallicities in the GEMS are probably already solar or greater, relying on gas-to-dust ratios as previously estimated by Magdis et al. (2011). Solar or greater gas-phase metallicities in massive, dusty starburst galaxies at redshifts $z \sim 2–3$ are also suggested by studies of warm ionized gas in these galaxies (Takata et al. 2006; Nesvadba et al. 2007), as well as by the abundances found in the photospheres of the dominant stellar populations in massive low-redshift galaxies, which probe the metallicities at the time when these stars were formed; they are solar or super-solar (Gallazzi et al. 2005), and also do not favor unusually low carbon abundances in the GEMS and other, similar high-redshift galaxies. This makes a much lower X_{CI} and a higher α_{CO} than the ULIRG-value implausible, at least for this type of high-redshift galaxy. For bluer, lower-mass, and less intensely star-forming galaxies, this is probably different, and overall, the range of α_{CO} is probably set by a range of parameters, including in particular metallicity (e.g., Bolatto et al. 2013).

Collecting large enough sets of emission lines of individual high-redshift galaxies to study their gas excitation in detail is often very challenging. To obtain these mass estimates, it was critical in our case to accurately take into account gas excitation when extrapolating from mid-J CO line luminosities to the luminosities of CO(1–0), since the line ratios are lower than others in the literature by factors of 1.5–2 (for details see C18). Had we used the higher values of for example Spilker et al. (2014) or Danielson et al. (2011), we would have been led to believe that we had found considerably higher molecular gas masses from [CI] 1–0 than from the mid-J CO lines. Figures 4 and 5 show that the GEMS as an ensemble have somewhat lower ratios of $L_{\mathrm{CI10}}/L_{\mathrm{CO43}}$, and somewhat higher ratios of $L_{\mathrm{CI10}}/L_{\mathrm{FIR}}$ compared to other populations of high- and low-redshift galaxies, which is consistent with this finding. This may indicate that their gas is perhaps somewhat denser or more highly excited than in other galaxies at the same redshifts, as also shown by C18, and as would be consistent with targeting particularly bright galaxies on the sub-millimeter sky. Despite these indications, they fall well within the scatter of the overall population.

If our results are applicable to more general populations of massive, dusty, high-redshift starburst galaxies, then this would imply that most of the discrepancy seen in mass estimates from [CI] and CO could be dominated by the diversity in average gas excitation of these galaxies. For example, similar effects could be at play for other samples of vigorous starburst galaxies showing enhanced carbon abundances, like those found with the SPT (Bothwell et al. 2017). The origin of this diversity may either be differences in the excitation process itself, or in the relative contribution of high and low-excitation gas (e.g., Ivison et al. 2010; Harris et al. 2010; Yang et al. 2017, C18). Even the largest ratios of $M_{\mathrm{H2,CI}}$ to $M_{\mathrm{H2,CO}}$ amongst the GEMS, namely $M_{\mathrm{H2,CI}}/M_{\mathrm{H2,CO}} = 1.7 \pm 0.2$, could reflect differences in gas excitation rather than additional gas components not seen in CO(1–0). For example, Papadopoulos & Greve (2004) state a range of a factor of three of plausible excitation parameters Q_{10} for molecular gas mass estimates from [CI] 1–0.

Regardless of these concerns, our results do suggest that CO(1–0) and [CI] 1–0 are probing similar gas reservoirs within the GEMS, and that the impact of differential lensing does not

Table 5. Diagnostic line ratios.

Source	CO transition	$\mu L'_{CO}{}^a$ (10^{11} K km s^{-1} pc^2)	$\mu L'_{CI10}$ (10^{11} K km s^{-1} pc^2)	L'_{CO}/L'_{CI10}
PLCK_G045.1+61.1	4–3	7.5 ± 0.9	2.3 ± 0.5	3.3 ± 0.8
PLCK_G080.2+49.8	3–2	2.9 ± 0.2	1.1 ± 0.2	2.6 ± 0.5
PLCK_G092.5+52.9	4–3	10.9 ± 0.7	3.3 ± 0.6	3.3 ± 0.6
PLCK_G102.1+53.6	3–2	2.2 ± 0.8	0.7^b	3.1
PLCK_G113.7+61.0	4–3	3.7 ± 0.3	1.5 ± 0.2	2.5 ± 0.4
PLCK_G138.6+62.0	4–3	4.9 ± 0.3	1.5 ± 0.2	3.3 ± 0.5
PLCK_G145.2+50.9	4–3	12.2 ± 2.4	4.2 ± 1.0	2.9 ± 0.9
PLCK_G165.7+67.0	4–3	4.6 ± 0.3	1.5 ± 0.4	3.1 ± 0.8
PLCK_G200.6+46.1	3–2	6.0 ± 0.6	1.3^b	4.6
PLCK_G231.3+72.2	3–2	5.5 ± 0.8	0.9^b	6.4
PLCK_G244.8+54.9	4–3	7.0 ± 0.7	3.1^b	2.3

Notes. [a]Taken from C18. [b]Estimated from [CI] 2–1, assuming a ratio $I_{CI1-0}/I_{CI2-1} = 1.8$, the average of the values of the four galaxies where we cover both lines. Error bars include the measurement uncertainties, and are only given for galaxies for which [CI] 1–0 has actually been measured.

Table 6. Molecular gas mass estimates derived from [CI] 1–0, and from CO.

Source	$\mu M_{H2,CI}{}^a$ ($10^{11} M_\odot$)	$\mu M_{H2,CO43,extr}{}^b$ ($10^{11} M_\odot$)	$M_{H2,CI}/M_{H2,CO10}{}^c$	$M_{CI}/M_{H2,CO43,extr}$	$X_{CI,CO10}$ ($\times 10^{-5}$)	$X_{CI,CO43,extr}$ ($\times 10^{-5}$)
PLCK_G045.1+61.1	20.9 ± 4.7	19.9 ± 2.4	…	1.0 ± 0.3	…	2.5 ± 0.5
PLCK_G080.2+49.8	9.8 ± 0.8	5.7 ± 0.4	…	1.7 ± 0.2	…	3.8 ± 0.9
PLCK_G092.5+52.9	30.9 ± 2.3	24.8 ± 1.6	1.1 ± 0.4	1.2 ± 0.1	2.7 ± 0.9	3.0 ± 0.3
PLCK_G113.7+61.0	14.2 ± 0.7	11.6 ± 0.9	1.4 ± 0.1	1.2 ± 0.1	3.2 ± 1.0	2.9 ± 0.6
PLCK_G138.6+62.0	13.4 ± 0.9	14.6 ± 0.9	1.1 ± 0.4	0.9 ± 0.1	2.6 ± 0.7	2.2 ± 0.4
PLCK_G145.2+50.9	38.9 ± 0.5	23.3 ± 0.9	…	1.7 ± 0.1	…	4.0 ± 0.7
PLCK_G165.7+67.0	13.5 ± 0.4	15.0 ± 0.4	0.95 ± 0.1	0.9 ± 0.1	2.3 ± 0.5	2.2 ± 0.3
PLCK_G244.8+54.9	…	14.0 ± 1.4	…	…	…	…

Notes. Ratios of mass estimates and carbon abundance, X_{CI}, for the different molecular gas mass estimates from CO. [a]For $X_{CI} = 3 \times 10^{-5}$, and $\alpha_{CO,ULIRG} = 0.8\, M_\odot$ / [K km s^{-1} pc^2]. [b]Using the average luminosity ratios of the GEMS, $R_{32} = L'_{CO(3-2)}/L'_{CO(1-0)} = 0.4$ and $L'_{CO(4-3)}/L'_{CO(1-0)} = 0.3$ (C18) to extrapolate to $L'_{CO(1-0)}$. [c]CO(1–0) is taken from Harrington et al. (2018), for $\alpha_{CO,ULIRG} = 0.8\, M_\odot$ / [K km s^{-1} pc^2].

dominate the observed luminosity and mass estimates derived from either line. In particular, and while we do see multiple gas components with different excitation conditions in the GEMS (C18), we find no evidence that such galaxies have large fractions of "CO-dark" cold, neutral gas, that would not be seen in CO(1–0).

6. Summary and conclusions

We have presented an analysis of the [CI] 1–0 and [CI] 2–1 emission lines in *Planck*'s Dusty GEMS, a small sample of 11 of the brightest high-redshift galaxies on the sub-millimeter sky observed with the *Planck* satellite. We have detailed lens models derived with LENSTOOL from sub-arcsecond interferometry for all galaxies (Cañameras et al. 2018b), and can therefore explicitly account for source morphology and differential lensing between dense gas and dust (finding that it does not play a major role). We detect all [CI] lines from those galaxies where these lines fall into the atmospheric windows. In total, we measured the [CI] 1–0 line in seven, and the [CI] 2–1 line in eight galaxies, measuring both lines for four galaxies. Our main results are as follows.

– The GEMS have [CI] line fluxes between 4 and 21 Jy km s^{-1}, with $L_{[CI]21+10}/L_{FIR}$ between 1.2×10^{-5} and 2.6×10^{-5}, comparable to, and in the lower range of, other galaxies at low and high redshift.
– Line ratios L_{CI21}/L_{CI10} are between 1.2 and 3.3, and the [CI] line emission is consistent with optically thin ($\tau =$

0.01–0.14) gas in star-forming regions dominated by UV heating, without major contribution from an AGN, and excitation temperatures of typically about $T_{ex} = 20$ K, with one galaxy having $T_{ex} = 36$ K.
– The line ratios of [CI] 1–0 and CO(4–3) are between 2.3 and 3.5. Following Greve et al. (2012) and Papadopoulos & Geach (2012) we interpret this as a sign that these galaxies are undergoing starbursts, not the more regular, longer-term star formation typical of disk galaxies at similar redshifts.
– The intrinsic masses of atomic carbon are between 0.8 and $6.3 \times 10^7\, M_\odot$, corresponding to atomic carbon abundances between $X_{CI} = 2 \times 10^{-5}$ and 4×10^{-5}. This is comparable to the usually adopted value of 3×10^{-5} initially derived for M82, and several other samples of high-redshift galaxies. However, recent studies have also found either higher (Bothwell et al. 2017) or lower values (Valentino et al. 2018), in either case within a factor of about two.
– H$_2$ gas mass estimates from [CI] 1–0 (and adopting a carbon abundance of 3×10^{-5}), correspond to those measured from CO within the measurement uncertainties for five of seven galaxies for which [CI] 1–0 has been measured, and within factors 1.7 for the other two. These values were derived for a standard "ULIRG" CO-to-H$_2$ conversion factor, $\alpha_{CO} = 0.8\, M_\odot$ / [K km s^{-1} pc^2], and from mid-J CO line observations (either $J = 4$–3 or $J = 3$–2) corrected for their

ratio with CO(1–0), as directly observed by Harrington et al. (2018) for four GEMS. These ratios are factors of 1.5–2 lower than previously proposed for other samples of massive, dusty starburst galaxies at comparable redshifts (Cañameras et al. 2018b), suggesting that the gas excitation conditions play a non-negligible role in molecular-gas mass estimates of dusty starburst galaxies at redshifts 2–4. Once excitation was properly taken into account, we found that the standard values of α_{CO}, atomic carbon abundances, and the [CI] excitation parameter $Q_{10} = 0.49$ together give consistent results for molecular gas mass estimates derived from [CI] and CO in these galaxies. Consequently, we do not see evidence for large gas reservoirs that are probed by [CI] but not CO.

References

Alaghband-Zadeh, S., Chapman, S. C., Swinbank, A. M., et al. 2013, MNRAS, 435, 1493
Andreani, P., Retana-Montenegro, E., Zhang, Z.-Y., et al. 2018, A&A, 615, A142
Balashev, S. A., Noterdaeme, P., Rahmani, H., et al. 2017, MNRAS, 470, 2890
Barvainis, R., Maloney, P., Antonucci, R., & Alloin, D. 1997, ApJ, 484, 695
Beuther, H., Bihr, S., Rugel, M., et al. 2016, A&A, 595, A32
Bisbas, T. G., Papadopoulos, P. P., & Viti, S. 2015, ApJ, 803, 37
Bisbas, T. G., van Dishoeck, E. F., Papadopoulos, P. P., et al. 2017, ApJ, 839, 90
Bolatto, A. D., Wolfire, M., & Leroy, A. K. 2013, ARA&A, 51, 207
Bothwell, M. S., Aguirre, J. E., Aravena, M., et al. 2017, MNRAS, 466, 2825
Brown, R. L., & Vanden Bout, P. A. 1992, ApJ, 397, L11
Cañameras, R., Nesvadba, N. P. H., Guery, D., et al. 2015, A&A, 581, A105
Cañameras, R., Nesvadba, N., Kneissl, R., et al. 2017a, A&A, 604, A117
Cañameras, R., Nesvadba, N. P. H., Kneissl, R., et al. 2017b, A&A, 600, L3
Cañameras, R., Nesvadba, N. P. H., Limousin, M., et al. 2018a, A&A, 620, A60
Cañameras, R., Yang, C., Nesvadba, N. P. H., et al. 2018b, A&A, 620, A61
Carilli, C. L., & Walter, F. 2013, ARA&A, 51, 105
Danielson, A. L. R., Swinbank, A. M., Smail, I., et al. 2011, MNRAS, 410, 1687
Frye, B. L., Pascale, M., Qin, Y., et al. 2019, ApJ, 871, 51
Gallazzi, A., Charlot, S., Brinchmann, J., White, S. D. M., & Tremonti, C. A. 2005, MNRAS, 362, 41
Geach, J. E., & Papadopoulos, P. P. 2012, ApJ, 757, 156
Gerin, M., & Phillips, T. G. 2000, ApJ, 537, 644
Gerin, M., Ruaud, M., Goicoechea, J. R., et al. 2015, A&A, 573, A30
Gildas Team 2013, Astrophysics Source Code Library [record ascl:1305.010]
Goldsmith, P. F., Langer, W. D., Pineda, J. L., & Velusamy, T. 2012, ApJS, 203, 13
Greve, T. R., Vieira, J. D., Weiß, A., et al. 2012, ApJ, 756, 101
Harrington, K. C., Yun, M. S., Magnelli, B., et al. 2018, MNRAS, 474, 3866
Harris, A. I., Baker, A. J., Zonak, S. G., et al. 2010, ApJ, 723, 1139
Hodge, J. A., Smail, I., Walter, F., et al. 2018, ApJ, submitted [arXiv:1810.12307]
Israel, F. P., & Baas, F. 2002, A&A, 383, 82
Israel, F. P., & Baas, F. 2003, A&A, 404, 495
Ivison, R. J., Magnelli, B., Ibar, E., et al. 2010, A&A, 518, L31
Ivison, R. J., Papadopoulos, P. P., Smail, I., et al. 2011, MNRAS, 412, 1913
Jiao, Q., Zhao, Y., Zhu, M., et al. 2017, ApJ, 840, L18
Jullo, E., & Kneib, J.-P. 2009, MNRAS, 395, 1319
Kamenetzky, J., Rangwala, N., Glenn, J., Maloney, P. R., & Conley, A. 2016, ApJ, 829, 93
Kaufman, M. J., Wolfire, M. G., Hollenbach, D. J., & Luhman, M. L. 1999, ApJ, 527, 795
Krips, M., Martín, S., Sakamoto, K., et al. 2016, A&A, 592, L3
Le Petit, F., Nehmé, C., Le Bourlot, J., & Roueff, E. 2006, ApJS, 164, 506
Magdis, G. E., Daddi, E., Elbaz, D., et al. 2011, ApJ, 740, L15
Markwardt, C. B. 2009, in Astronomical Data Analysis Software and Systems XVIII, eds. D. A. Bohlender, D. Durand, & P. Dowler, ASP Conf. Ser., 411, 251
Meijerink, R., Spaans, M., & Israel, F. P. 2007, A&A, 461, 793
Nesvadba, N. P. H., Lehnert, M. D., Genzel, R., et al. 2007, ApJ, 657, 725
Nesvadba, N., Kneissl, R., Cañameras, R., et al. 2016, A&A, 593, L2
Offner, S. S. R., Bisbas, T. G., Bell, T. A., & Viti, S. 2014, MNRAS, 440, L81
Papadopoulos, P. P., & Geach, J. E. 2012, ApJ, 757, 157
Papadopoulos, P. P., & Greve, T. R. 2004, ApJ, 615, L29
Papadopoulos, P. P., Thi, W.-F., & Viti, S. 2004, MNRAS, 351, 147
Phillips, T. G., & Huggins, P. J. 1981, ApJ, 251, 533
Roueff, E., & Flower, D. R. 1992, MNRAS, 258, 45P
Planck Collaboration XVI. 2014, A&A, 571, A16
Planck Collaboration Int. XXVII. 2015, A&A, 582, A30
Planck Collaboration Int. XXXIX. 2016, A&A, 596, A100
Rémy-Ruyer, A., Madden, S. C., Galliano, F., et al. 2015, A&A, 582, A121
Riechers, D. A., Bradford, C. M., Clements, D. L., et al. 2013, Nature, 496, 329
Rosenberg, M. J. F., van der Werf, P. P., Aalto, S., et al. 2015, ApJ, 801, 72
Schneider, N., Simon, R., Kramer, C., et al. 2003, A&A, 406, 915
Solomon, P. M., Downes, D., Radford, S. J. E., & Barrett, J. W. 1997, ApJ, 478, 144
Solomon, P. M., & Vanden Bout, P. A. 2005, ARA&A, 43, 677
Spilker, J. S., Marrone, D. P., Aguirre, J. E., et al. 2014, ApJ, 785, 149
Swinbank, A. M., Papadopoulos, P. P., Cox, P., et al. 2011, ApJ, 742, 11
Tacconi, L. J., Genzel, R., Smail, I., et al. 2008, ApJ, 680, 246
Takata, T., Sekiguchi, K., Smail, I., et al. 2006, ApJ, 651, 713
Valentino, F., Magdis, G. E., Daddi, E., et al. 2018, ApJ, 869, 27
Vieira, J. D., Marrone, D. P., Chapman, S. C., et al. 2013, Nature, 495, 344
Wagg, J., Wilner, D. J., Neri, R., Downes, D., & Wiklind, T. 2006, ApJ, 651, 46
Walter, F., Weiß, A., Downes, D., Decarli, R., & Henkel, C. 2011, ApJ, 730, 18
Wardlow, J. L., Cooray, A., De Bernardis, F., et al. 2013, ApJ, 762, 59
Weiß, A., Neininger, N., Hüttemeister, S., & Klein, U. 2001, A&A, 365, 571
Weiß, A., Downes, D., Walter, F., & Henkel, C. 2005a, A&A, 440, L45
Weiß, A., Downes, D., Henkel, C., & Walter, F. 2005b, A&A, 429, L25
Wolfire, M. G., Hollenbach, D., & McKee, C. F. 2010, ApJ, 716, 1191
Yang, C., Omont, A., Beelen, A., et al. 2017, A&A, 608, A144

1. Institut d'Astrophysique Spatiale, CNRS, Université Paris-Sud, Université Paris-Saclay, 91405 Orsay, France
   e-mail: `nicole.nesvadba@ias.u-psud.fr`
2. Dark Cosmology Centre, Niels Bohr Institute, University of Copenhagen, Juliane Maries Vej 30, 2100 Copenhagen, Denmark
3. European Southern Observatory, ESO Vitacura, Alonso de Cordova 3107, Vitacura, Casilla 19001, Santiago, Chile
4. Atacama Large Millimeter/submillimeter Array, ALMA Santiago Central Offices, Alonso de Cordova 3107, Vitacura, Cailla 763-0355, Santiago, Chile
5. Chalmers University of Technology, Onsala Space Observatory, Onsala, Sweden
6. Laboratoire AIM, CEA/DSM/IRFU, CNRS, Université Paris-Diderot, Bât 709, 91191 Gif-sur-Yvette, France
7. Institut d'Astrophysique de Paris, UPMC Université Paris 06, UMR 7095, 75014 Paris, France
8. Department of Physics and Astronomy, University of British Columbia, 6224 Agricultural Road, Vancouver 6658, British Columbia, Canada